

Properties of $K^\pi = 0_1^+$, $K^\pi = 2^-$, and $K^\pi = 0_1^-$ bands of ^{20}Ne probed via proton and alpha inelastic scattering

Yoshiko Kanada-En'yo

Department of Physics, Kyoto University, Kyoto 606-8502, Japan

Kazuyuki Ogata

Research Center for Nuclear Physics (RCNP), Osaka University, Ibaraki 567-0047, Japan

Department of Physics, Osaka City University, Osaka 558-8585, Japan and

Nambu Yoichiro Institute of Theoretical and Experimental Physics (NITEP), Osaka City University, Osaka 558-8585, Japan

The $K^\pi = 0_1^+$, $K^\pi = 2^-$, and $K^\pi = 0_1^-$ bands of ^{20}Ne are investigated with microscopic structure and reaction calculations via proton and α inelastic scattering off ^{20}Ne . Structures of ^{20}Ne are calculated with variation after parity and total angular momentum projections in the antisymmetrized molecular dynamics (AMD). The $K^\pi = 0_1^+$ and $K^\pi = 0_1^-$ bands have $^{16}\text{O} + \alpha$ cluster structures, whereas the $K^\pi = 2^-$ band shows a $^{12}\text{C} + 2\alpha$ -like structure. Microscopic coupled-channel calculations of proton and α scattering off ^{20}Ne are performed by using the proton-nucleus and α -nucleus potentials, which are derived by folding the Melbourne g -matrix NN interaction with AMD densities of ^{20}Ne . The calculation reasonably reproduces the observed cross sections of proton scattering at $E_p = 25\text{--}35$ MeV and α scattering at $E_\alpha = 104\text{--}386$ MeV. Transition properties from the ground to excited states are discussed by reaction analyses of proton and α inelastic processes. Mixing of the $K^\pi = 2^-$ and $K^\pi = 0_1^-$ bands is discussed by detailed analysis of the $0_1^+ \rightarrow 3_1^-$ and $0_1^+ \rightarrow 3_2^-$ transitions. For the 3_1^- state, mixing of the $K^\pi = 0_1^-$ cluster component in the $K^\pi = 2^-$ band plays an important role in the transition properties.

I. INTRODUCTION

Cluster structure plays an important role in nuclei, in particular, in light-mass regions. A typical cluster structure in sd -shell nuclei is $^{16}\text{O} + \alpha$ cluster structure of ^{20}Ne [1]. The idea of the $^{16}\text{O} + \alpha$ cluster structure has been introduced to describe energy levels of the parity-doublet $K^\pi = 0_1^+$ and $K^\pi = 0_1^-$ bands [2], and extended to describe the higher nodal $^{16}\text{O} + \alpha$ cluster band assigned as the $K^\pi = 0_4^+$ (labeled as $K^\pi = 0_{\text{hn}}^+$) band. The structure and α -decay properties of $^{16}\text{O} + \alpha$ cluster states have been intensively investigated with potential models and (semi)microscopic cluster models [1, 3–14].

In excited states of ^{20}Ne , further rich phenomena beyond the $^{16}\text{O} + \alpha$ cluster structure arise from cluster breaking, i.e., internal excitation of ^{16}O and α clusters. For example, in the $K^\pi = 0_1^+$ band, the cluster breaking is essential to describe deviation from ideal rotational spectra at the band terminal [15–17]. In addition, $^{12}\text{C} + 2\alpha$ (or $^{12}\text{C} + ^8\text{Be}$) cluster structure has been considered to discuss the $K^\pi = 0_2^+$ and $K^\pi = 0_3^+$ bands, in the frameworks of extended cluster models [6, 9–11] and antisymmetrized molecular dynamics (AMD) [18]. The cluster structures of ^{20}Ne have been also discussed with mean-field approaches [19–22]. Moreover, the lowest negative-parity band experimentally assigned as the $K^\pi = 2^-$ band is considered to be a particle-hole state or octupole Y_{32} vibration [11, 16, 19, 20, 23].

It means that two types of negative-parity states appear in low-energy levels of ^{20}Ne , the mean-field type states in the $K^\pi = 2^-$ band and the $^{16}\text{O} + \alpha$ cluster states in the $K^\pi = 0_1^-$ band. The former band arises from the $K^\pi = 2^-$ particle-hole excitation, and the latter is caused by the $K^\pi = 0^-$ excitation of the inter-

cluster motion between ^{16}O and α clusters. In the experimental levels, the 3_1^- (5.62 MeV) and 3_2^- (7.16 MeV) states are assigned to the $K^\pi = 2^-$ and $K^\pi = 0_1^-$ bands, respectively. Energy levels and in-band $E2$ transitions in each band have been reproduced well by theoretical calculations with the $(^{16}\text{O} + \alpha) + (^{12}\text{C} + ^8\text{Be})$ coupled-channel orthogonal condition model (CC-OCM) [11] and the deformed-basis AMD (def-AMD) [16]. However, the observed $E3$ transition strength, $B(E3; 3_1^- \rightarrow 0_1^+)$ [24], for the inter-band transition from the $K^\pi = 2^-$ band to the ground band is much larger by one order of magnitude than the theoretical value of CC-OCM, and inconsistent with the simple interpretation of the $K^\pi = 2^-$ band as the particle-hole excitation.

In order to investigate structure and transition properties of the ground and excited bands, electron and hadron scattering experiments have been performed for sd -shell nuclei. For ^{20}Ne , hadron inelastic scattering such as (p, p') and (α, α') have been investigated [25–31]. Phenomenological reaction analyses of the (p, p') and (d, d') cross sections have suggested again the strong $3_1^- \rightarrow 0_1^+$ transition consistently with the $B(E3; 3_1^- \rightarrow 0_1^+)$ data determined by γ decays, but the $B(E3; 3_1^- \rightarrow 0_1^+)$ values evaluated from hadron scattering show dependence on energies and projectile particles.

In principle, proton and α inelastic scattering can be good probes for transition properties from the ground to excited states provided that reliable reaction analyses are available. Recently, microscopic coupled-channel (MCC) calculations for proton and α scattering have been remarkably developed. In the MCC calculations, matter and transition densities of target nuclei obtained with microscopic structure models are utilized as inputs of coupled-channel reaction calculations in microscopic

folding models (MFMs), in which nucleon-nucleus and α -nucleus potentials are constructed by folding effective NN interactions. In our previous studies [32–35], we have applied the MCC calculations to proton and α scattering off various target nuclei in the p - and sd -shell regions with structure model calculation of AMD. Using the Melbourne g -matrix NN interaction [36], we have succeeded in reproducing (p, p') and (α, α') cross sections of various excited states such as cluster and vibration excitations. The Melbourne g -matrix interaction is an effective NN interaction in nuclear medium based on a bare NN interaction of the Bonn B potential [37]. Owing to the fundamental derivation, it contains energy and density dependences in the applicable range without relying on phenomenological adjustment of interaction parameters.

In the present study, we calculate structure of ^{20}Ne with variation after parity and angular-momentum projections (VAP) in the AMD framework [38–40]. We, then, apply the MCC approach to proton and α scattering off ^{20}Ne with the Melbourne g -matrix NN interaction using AMD densities of ^{20}Ne as structure inputs of the target nucleus. With analyses of the structure and reaction calculations, structures of the ground and excited states in the $K^\pi = 0_1^+$, $K^\pi = 2^-$, and 0_1^- bands are investigated. In particular, properties of the 3_1^- and 3_2^- states and possible mixing of the $K^\pi = 2^-$ and $K^\pi = 0_1^-$ bands are discussed in detail.

The paper is organized as follows. The next section describes the frameworks of the AMD calculation of ^{20}Ne and the MCC approach for proton and α scattering off ^{20}Ne . Structure properties are described in Sec. III, and the results of proton and α scattering are shown in Sec. IV. A discussion of the 3_1^- and 3_2^- states is given in Sec. V. Finally the paper is summarized in Sec. VI.

II. METHOD

A. Structure calculations of ^{20}Ne

We apply the VAP version of AMD to calculate structure of ^{20}Ne . The method is almost the same as those used for studies of ^{12}C and neutron-rich Be isotopes in Refs. [39, 41, 42]. It is sometimes called AMD+VAP, but we simply call it AMD in the present paper. For comparison, we also apply a $^{16}\text{O} + \alpha$ -cluster model with the generator coordinate method (GCM) [43, 44].

In the framework of AMD, an A -nucleon wave function is given by a Slater determinant of single-nucleon

Gaussian wave functions as

$$\Phi_{\text{AMD}}(\mathbf{Z}) = \frac{1}{\sqrt{A!}} \mathcal{A}\{\varphi_1, \varphi_2, \dots, \varphi_A\}, \quad (1)$$

$$\varphi_i = \phi_{\mathbf{X}_i} \chi_i \tau_i, \quad (2)$$

$$\phi_{\mathbf{X}_i}(\mathbf{r}_j) = \left(\frac{2\nu}{\pi}\right)^{3/4} \exp[-\nu(\mathbf{r}_j - \mathbf{X}_i)^2], \quad (3)$$

$$\chi_i = \left(\frac{1}{2} + \xi_i\right) \chi_\uparrow + \left(\frac{1}{2} - \xi_i\right) \chi_\downarrow. \quad (4)$$

Here \mathcal{A} is the antisymmetrizer, and φ_i is the i th single-particle wave function written by a product of spatial ($\phi_{\mathbf{X}_i}$), spin (χ_i), and isospin (τ_i fixed to be proton or neutron) wave functions. The width parameter ν is chosen to be $\nu = 0.19 \text{ fm}^{-2}$ for all nucleons as the same as that used for AMD+VAP calculations of ^{12}C and ^{16}O in Refs. [39, 45]. Parameters $\mathbf{Z} \equiv \{\mathbf{X}_1, \dots, \mathbf{X}_A, \xi_1, \dots, \xi_A\}$, which represent Gaussian centroid positions and nucleon-spin orientations, are optimized by the energy variation for each J^π state of ^{20}Ne so as to minimize the energy expectation value $E = \langle \Psi | \hat{H} | \Psi \rangle / \langle \Psi | \Psi \rangle$ with respect to the parity and total angular momentum projected wave functions $\Psi = P_{MK}^{J^\pi} \Phi_{\text{AMD}}(\mathbf{Z})$. Here $P_{MK}^{J^\pi}$ is the parity and total angular momentum projection operator.

The VAP is performed for $J^\pi = \{0^+, 2^+, 4^+\}$, $\{2^-, 3^-, 4^-\}$, and $\{1^-, 3^-\}$ by choosing $K = 0$, $K = 2$, and $K = 0$, respectively. For each band, firstly the band-head state is obtained by the VAP from a randomly chosen initial state, and then higher angular momentum states are calculated by the VAP from the initial wave function projected from $\Phi_{\text{AMD}}(\mathbf{Z})$ obtained for the band-head state. Totally eight AMD wave functions $\Phi_{\text{AMD}}(\mathbf{Z}^{(m)})$ ($m = 1, \dots, 8$) are obtained after the VAP, and all of them are superposed to obtain final wave functions of the ground and excited states of ^{20}Ne . Namely, for the basis wave functions $P_{MK}^{J^\pi} \Phi_{\text{AMD}}(\mathbf{Z}^{(m)})$ projected from the intrinsic wave functions, the diagonalization of Hamiltonian and norm matrices is done to obtain J^π states. The diagonalization is done with respect to K and m meaning the K -mixing and the configuration (m) mixing. As a result of the diagonalization, $J^\pi = \{0^+, 2^+, 4^+\}$ states in the $K^\pi = 0_{\text{hn}}^+$ band are also obtained.

The effective nuclear interactions used in the present AMD calculation are the same as those in Refs. [39, 45]. The MV1 (case 1) central force [46] with the parameters $(b, h, m) = (0, 0, 0.62)$ and the spin-orbit term of the G3RS force [47, 48] with the strength parameters $u_{ls} \equiv u_l = -u_{ll} = 3000 \text{ MeV}$ are used. The Coulomb force is also included.

The AMD calculation of ^{20}Ne with this set of interactions obtains reasonable results of energy levels and in-band transitions of the $K^\pi = 0_1^+$, $K^\pi = 0_1^-$, and $K^\pi = 0_{\text{hn}}^+$ bands but it gives a higher energy of the $K^\pi = 2^-$ band than the $K^\pi = 0_1^-$ band, which is inverse ordering of the $K^\pi = 2^-$ and $K^\pi = 0_1^-$ bands compared with experimental levels. The excitation energy of the $K^\pi = 2^-$ band is sensitive to the strength

of spin-orbit interactions as discussed in Refs. [16, 19]. We can improve the $K^\pi = 2^-$ energy with a slight modification of the spin-orbit strength and obtain the correct ordering of the $K^\pi = 2^-$ and $K^\pi = 0_1^-$ bands. In order to discuss possible state mixing between the $K^\pi = 2^-$ and $K^\pi = 0_1^-$ bands, we also use a strength of $u_{ls} = 3400$ MeV modified from the original value $u_{ls} = 3000$ MeV, and perform diagonalization of the basis AMD wave functions already obtained by VAP with the default strength ($u_{ls} = 3000$ MeV). We label the AMD calculation with the default and modified strengths, $u_{ls} = 3000$ MeV and 3400 MeV, as AMD and AMD-ls34, respectively.

In addition to the AMD calculation, a structure calculation of the $^{16}\text{O} + \alpha$ -cluster model (CM) is also performed with GCM. In the GCM framework, the Brink-Bloch $^{16}\text{O} + \alpha$ -cluster wave functions [49] with inter-cluster distances of 1, 2, ..., 10 fm are superposed. In the CM calculation, we adopt the same parametrization as that used in the $^{16}\text{O} + \alpha$ -cluster model calculation with the resonating group method in Refs. [7, 8]. That is, the width parameter of $\nu = 0.16 \text{ fm}^{-2}$ of ^{16}O and α clusters and the Volkov No.2 central nuclear interaction with $m = 0.62$ are used.

B. MCC calculation of proton and α scattering off ^{20}Ne

Elastic and inelastic cross sections of proton and α scattering off ^{20}Ne are calculated with the MCC approach as done in our previous studies of Refs. [32–35]. For the details of the reaction calculations, the reader is referred to those references.

The nucleon-nucleus potentials are constructed in a MFM, where the diagonal and coupling potentials are calculated by folding the Melbourne g -matrix NN interaction [36] with matter and transition densities of the target nucleus. The α -nucleus potentials are obtained in an extended nucleon-nucleus folding (NAF) model [50] by folding the calculated nucleon-nucleus potentials with an α density.

The Melbourne g matrix is an effective NN interaction derived with a bare NN interaction of the Bonn B potential [37]. It contains energy and density dependences with no adjustable parameter, and works well in application for systematic description of proton elastic and inelastic scattering off various nuclei at energies $E_p = 40\text{--}300$ MeV [34–36, 51–53] and also α elastic and inelastic scattering at energies $E_\alpha = 100\text{--}400$ MeV [32, 33, 35, 50, 54]. In the present calculation of the proton-nucleus potentials, the spin-orbit term of the potential is not taken into account to avoid complexity as in Refs. [34, 35].

As structure inputs for the target nucleus, the matter ($\rho(r)$) and transition ($\rho^{\text{tr}}(r)$) densities of ^{20}Ne obtained by the AMD and CM calculations are used. $J^\pi = 0^+$, 1^- , 2^+ , 3^- , and 4^+ states in the $K^\pi = 0_1^+$, $K^\pi = 2^-$, $K^\pi = 0_1^-$, and $K^\pi = 0_{\text{hn}}^+$ bands and $\lambda \leq 4$ transitions between them are adopted in the MCC+AMD cal-

ulation, and those in the $K^\pi = 0_1^+$, $K^\pi = 0_1^-$, and $K^\pi = 0_{\text{hn}}^+$ bands are used in the MCC+CM calculation. In order to reduce model ambiguity from the structure calculation, the theoretical transition densities obtained by the structure calculations are renormalized in application to the MCC calculations so as to fit the experimental transition strengths as $\rho^{\text{tr}}(r) \rightarrow f^{\text{tr}}\rho^{\text{tr}}(r)$. Here the factor f^{tr} is determined with the squared ratio of experimental ($B_{\text{exp}}(E\lambda)$) to theoretical ($B_{\text{th}}(E\lambda)$) strengths as $f^{\text{tr}} = \sqrt{B_{\text{exp}}(E\lambda)/B_{\text{th}}(E\lambda)}$ for known values of $B_{\text{exp}}(E\lambda)$, and $f^{\text{tr}} = 1$ (no renormalization) is used for unknown cases.

III. STRUCTURE OF ^{20}Ne

The calculated energy levels of ^{20}Ne obtained by AMD, AMD-ls34, and CM are shown in Figs. 1(a), (b), and (c), respectively, and the experimental levels assigned to the $K^\pi = 0_1^+$, $K^\pi = 2^-$, $K^\pi = 0_1^-$, and $K^\pi = 0_{\text{hn}}^+$ bands are shown in Fig. 1 (d). The AMD calculation reasonably describes the experimental energy levels of the $K^\pi = 0_1^+$, $K^\pi = 0_1^-$, and $K^\pi = 0_{\text{hn}}^+$ bands (Fig. 1(a)). However, it overestimates the $K^\pi = 2^-$ levels and gives inverse ordering of the $K^\pi = 2^-$ and $K^\pi = 0_1^-$ bands compared with the experimental levels. In the AMD-ls34 result with a modified spin-orbit strength (Fig. 1 (b)), the excitation energy of the $K^\pi = 2^-$ band comes down lower than the $K^\pi = 0_1^-$ band, and correct ordering of the two negative-parity bands is obtained. As a result, the state mixing between the $K^\pi = 2^-$ and $K^\pi = 0_1^-$ bands occurs in the 3^- states in the AMD-ls34 case. This state mixing is not obtained in the default AMD calculation. In the result of CM, the energy levels of the $K^\pi = 0_1^+$, $K^\pi = 0_1^-$, and $K^\pi = 0_{\text{hn}}^+$ bands are reproduced, but the $K^\pi = 2^-$ band is missing because the $^{16}\text{O} + \alpha$ model space contains only axial symmetric configurations with pure $K = 0$ components.

In Table I, the calculated values of excitation energies (E_x) and root-mean-square radii (R) of ^{20}Ne obtained with AMD and CM are listed together with the experimental excitation energies. Experimentally, the $J^\pi = \{0_1^+, 2_1^+, 4_1^+\}$, $\{2_1^-, 3_1^-, 4_1^-\}$, and $\{1_1^-, 3_2^-\}$ states with strong in-band $E2$ transitions are assigned to the $K^\pi = 0_1^+$, $K^\pi = 2^-$, and $K^\pi = 0_1^-$ bands, respectively. Following this experimental assignment, we use the label 3_1^- (3_2^-) for the $K^\pi = 2^-$ ($K^\pi = 0_1^-$) band member of the theoretical results. The negative-parity states in the $K^\pi = 0_1^-$ band have large radii compared to the $K^\pi = 0_1^+$ and $K^\pi = 2^-$ bands because of a spatially developed $^{16}\text{O} + \alpha$ structure.

Figure 2 shows intrinsic density distribution of the basis AMD wave functions for the band-head states, 0_1^+ ($K^\pi = 0_1^+$), 2_1^- ($K^\pi = 2^-$), and 1_1^- ($K^\pi = 0_1^-$). In the three states, one or two α clusters are formed. The 0_1^+ ($K^\pi = 0_1^+$) state shows an $^{16}\text{O} + \alpha$ like structure, whereas the 1_1^- ($K^\pi = 0_1^-$) state has the most prominent $^{16}\text{O} + \alpha$ cluster structure. Qualitatively, these two bands

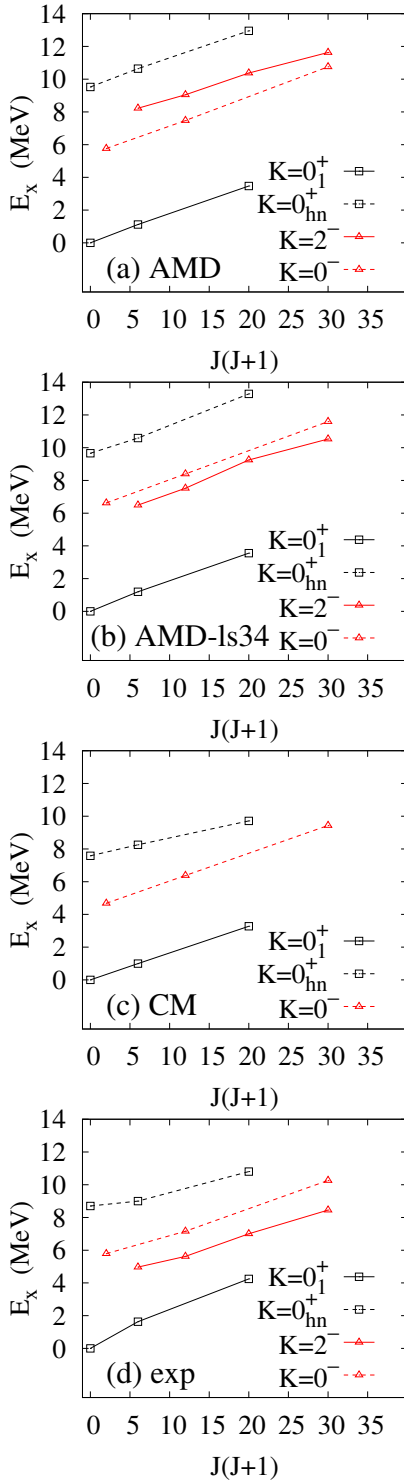


FIG. 1: The calculated energy levels of ^{20}Ne obtained by (a) AMD, (b) AMD-ls34, and (c) CM, and (d) the experimental levels assigned to the $K^\pi = 0_1^+$, $K^\pi = 2^-$, $K^\pi = 0_1^-$, and $K^\pi = 0_{\text{hn}}^+$ bands.

can be regarded as the parity doublets constructed from the $^{16}\text{O} + \alpha$ -cluster structure as in a simple $^{16}\text{O} + \alpha$ -

TABLE I: Excitation energies (E_x) and root-mean-square matter radii (R) of ^{20}Ne . The calculated values obtained with the AMD and CM calculations and the experimental values are listed. The experimental value of the point-proton rms radius of the ground state is $R = 2.888(2)$ fm from the charge radius data[56].

	exp	AMD		CM	
J^π	E_x (MeV)	E_x (MeV)	R (fm)	E_x (MeV)	R (fm)
$K^\pi = 0_1^+$					
0_1^+	0	0.0	3.01	0.0	2.95
2_1^+	1.634	1.1	3.01	1.0	2.94
4_1^+	4.248	3.5	2.99	3.3	2.92
$K^\pi = 2^-$					
2_1^-	4.967	8.2	2.94		
3_1^-	5.621	9.0	2.96		
4_1^-	7.004	10.4	2.97		
$K^\pi = 0_1^-$					
1_1^-	5.788	5.8	3.20	4.7	3.20
3_2^-	7.156	7.5	3.19	6.4	3.22

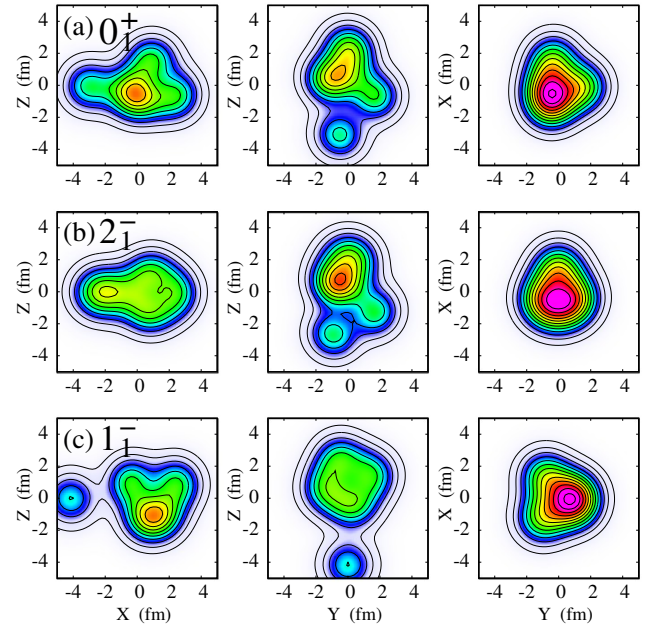


FIG. 2: Density distribution of intrinsic wave functions for the band-head states, (a) 0_1^+ , (b) 2_1^- , and (c) 1_1^- of the $K^\pi = 0_1^+$, $K^\pi = 2^-$, and $K^\pi = 0_1^-$ bands of ^{20}Ne obtained with AMD. The density projected onto X - Z , Y - Z , and Y - X planes are shown in left, middle, and right panels, respectively. Intrinsic axes are chosen as $\langle ZZ \rangle \geq \langle YY \rangle \geq \langle XX \rangle$ and $\langle XY \rangle = \langle YZ \rangle = \langle ZX \rangle = 0$.

cluster model, but strictly speaking it is not correct because the 0_1^+ ($K^\pi = 0_1^+$) state contains a deformed ^{16}O cluster showing a significant component of internal excitation of the cluster. The $K^\pi = 2^-$ band shows a

TABLE II: $E2$ transition strengths for in-band transitions in the $K^\pi = 0_1^+$, $K^\pi = 2^-$, and $K^\pi = 0_1^-$ bands, $E\lambda$ and isoscalar dipole (IS1) transition strengths to the ground state, and electric quadrupole moment (Q) of the 2_1^+ state. The theoretical values obtained by the AMD (default), AMD-ls34 (modified spin-orbit strength), and CM calculations are listed together with the experimental values from Refs. [24, 57]. Theoretical values of the ($^{16}\text{O} + \alpha$)+($^{12}\text{C} + ^8\text{Be}$) coupled-channel OCM (CC-OCM) [11] and the deformed-basis AMD (def-AMD) [16] are also shown. In addition, the $B(E\lambda)$ values reduced from inelastic scattering data of (e, e') [58], (p, p') at 800 MeV [29], 24.5 MeV [26, 28], and (d, d') at 52 MeV [25] are also shown. The units are $e^2\text{fm}^{2\lambda}$ for $B(E\lambda)$, $e^2\text{fm}^6$ for $B(\text{IS1})$, and efm^2 for Q .

	Exp.[24, 57]	CM	AMD	AMD-ls34	CC-OCM[11]	def-AMD[16]
$B(E2; 2_1^+ \rightarrow 0_1^+)$	65.4(3.2)	53	69	63	57.0	70.3
$B(E2; 4_1^+ \rightarrow 2_1^+)$	71(6)	67	92	84	70.9	83.7
$B(E2; 3_1^- \rightarrow 2_1^-)$	113(29)		95	89	107.5	102.8
$B(E2; 4_1^- \rightarrow 3_1^-)$	77(16)		79	68	77.0	77.8
$B(E2; 4_1^- \rightarrow 2_1^-)$	34(6)		32	31	34.0	38.5
$B(E2; 3_2^- \rightarrow 1_1^-)$	161(26)	178	163	150		151.2
$B(E3; 3_1^- \rightarrow 0_1^+)$	260(90)		53	155	29.9	
$B(E3; 3_2^- \rightarrow 0_1^+)$		543	548	335		
$B(\text{IS1}; 1_1^- \rightarrow 0_1^+)/4$		222	164	129		
$B(E4; 4_1^+ \rightarrow 0_1^+)$		5060	9270	7440		
$Q(2_1^+)$	-23(3)	-14.7	-16.9	-16.0	-15.2	
	(e, e')[58]	(p, p')[29]	(p, p')[26, 28]	(d, d')[25]		
		800 MeV	24.5 MeV	52 MeV		
$B(E2; 2_1^+ \rightarrow 0_1^+)$	71	52	66			
$B(E4; 4_1^+ \rightarrow 0_1^+)$	8100	5530	15200			
$B(E3; 3_1^- \rightarrow 0_1^+)$		300	450	420		
$B(E3; 3_2^- \rightarrow 0_1^+)$		146	230	450		

$^{12}\text{C} + 2\alpha$ -like structure with an axial asymmetric shape, where two α clusters are formed around a ^{12}C cluster. As a result of formation of the ^{12}C cluster, the $K^\pi = 2^-$ band gains the spin-orbit interaction. Compared to the $K^\pi = 0_1^-$ band, the $K^\pi = 2^-$ band has a compact structure with a mean-field aspect of particle-hole excitation on the prolate state. It means that the $K^\pi = 2^-$ band has the duality of cluster and mean-field features.

The results of electric ($E\lambda$) and isoscalar dipole (IS1) transition strengths and electric quadrupole moment (Q) are shown in Table II. The theoretical values obtained by AMD, AMD-ls34, and CM are shown together with the experimental data from Refs. [24, 57]. Moreover, theoretical values of the CC-OCM [11] and def-AMD [16] calculations are also shown for comparison. In addition to the experimental $B(E\lambda)$ measured by γ decays, the values reduced from (e, e') scattering data [58] and those evaluated from inelastic scattering of (p, p') [26, 28, 29] and (d, d') [25] are also shown in Table II. Note that uncertainty remains in the evaluation with hadron scattering because it relies on the phenomenological reaction analysis and shows significant dependences on energy and

projectile.

The observed in-band $E2$ transitions in the $K^\pi = 0_1^+$, $K^\pi = 2^-$, and $K^\pi = 0_1^-$ bands are reproduced well by the AMD calculation. The agreement is almost the same quality as other theoretical calculations of CC-OCM and def-AMD. The experimental Q moment of the 2_1^+ state is somewhat underestimated by the AMD and CM calculations.

For the $E4$ transition in the $K^\pi = 0_1^+$ band, the strength $B(E4; 4_1^+ \rightarrow 0_1^+)$ obtained with the AMD calculation is consistent with the (e, e') scattering, while the CM calculation gives a weaker $E4$ transition. The values evaluated from (p, p') scattering strongly depend on energies and have large uncertainty. For $E3$ transitions from the $K^\pi = 0_1^-$ band, AMD and CM give the remarkably strong $3_2^- \rightarrow 0_1^+$ transition because of the developed $^{16}\text{O} + \alpha$ -cluster structure. For the transition from the $K^\pi = 2^-$ band, the AMD calculation obtains the weak $3_1^- \rightarrow 0_1^+$ transition as one order of magnitude smaller strength as the $3_2^- \rightarrow 0_1^+$ strength. These AMD results of $B(E3; 3_1^- \rightarrow 0_1^+)$ and $B(E3; 3_2^- \rightarrow 0_1^+)$ are consistent with the CC-OCM calculation, but not consistent

with the observation. The observed $B(E3; 3_1^- \rightarrow 0_1^+)$ is much larger than the AMD and CC-OCM results. Moreover, the evaluation from (p, p') and (d, d') scattering suggests the same order transitions to the $3_1^-(K^\pi = 2^-)$ and $3_2^-(K^\pi = 0_1^-)$ states though uncertainty still remains.

Transition properties from the 0_1^+ state to the $3_1^-(K^\pi = 2^-)$ and $3_2^-(K^\pi = 0_1^-)$ states are sensitive to the state mixing between the $K^\pi = 2^-$ and $K^\pi = 0_1^-$ bands. Let us discuss effects of the state mixing on the $E3$ transition strengths by comparing the AMD-ls34 and AMD results for the cases with and without state mixing, respectively. As shown in Table II, the $B(E3; 3_1^- \rightarrow 0_1^+)$ value of AMD-ls34 is as three times large as that of AMD because of mixing of the $K^\pi = 0_1^-$ cluster component in the 3_1^- state. On the other hand, the $B(E3; 3_2^- \rightarrow 0_1^+)$ value decreases in the AMD-ls34 result compared to AMD because of destructive mixing of the $K^\pi = 2^-$ component in the 3_2^- state. In order to describe the experimental $B(E3; 3_1^- \rightarrow 0_1^+)$, the state mixing case of AMD-ls34 seems more likely than the almost no mixing case of AMD. Such the significant mixing may originate in coupling of the $^{12}\text{C}+2\alpha$ and $^{16}\text{O}+\alpha$ cluster structures contained in the $K^\pi = 2^-$ and $K^\pi = 0_1^-$ bands, respectively, as follows. The $^{16}\text{O}+\alpha$ cluster structure can be smoothly transformed into the $^{12}\text{C}+2\alpha$ with internal excitation of the ^{16}O cluster. Owing to this cluster degree of freedoms between the $^{16}\text{O}+\alpha$ and $^{12}\text{C}+2\alpha$ channels, the 3^- excitations in two channels can couple with each other.

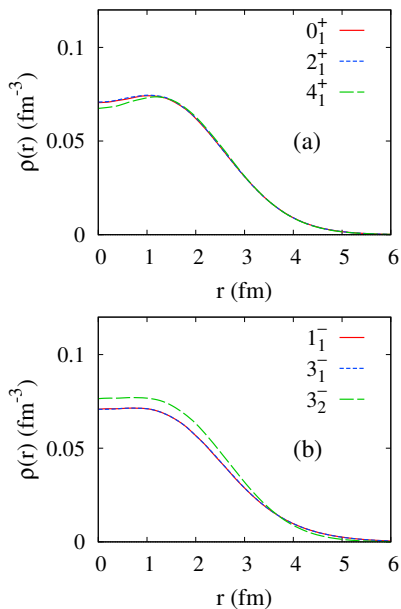


FIG. 3: Matter densities of ^{20}Ne calculated with AMD.

The calculated matter densities are shown in Fig. 3. Compared to the $K^\pi = 0_1^+$ and $K^\pi = 2^-$ bands, the 1_1^- and 3_2^- states in the $K^\pi = 0^-$ band show relatively broader density distribution in the outer region because of the developed $^{16}\text{O}+\alpha$ cluster structure, but the state

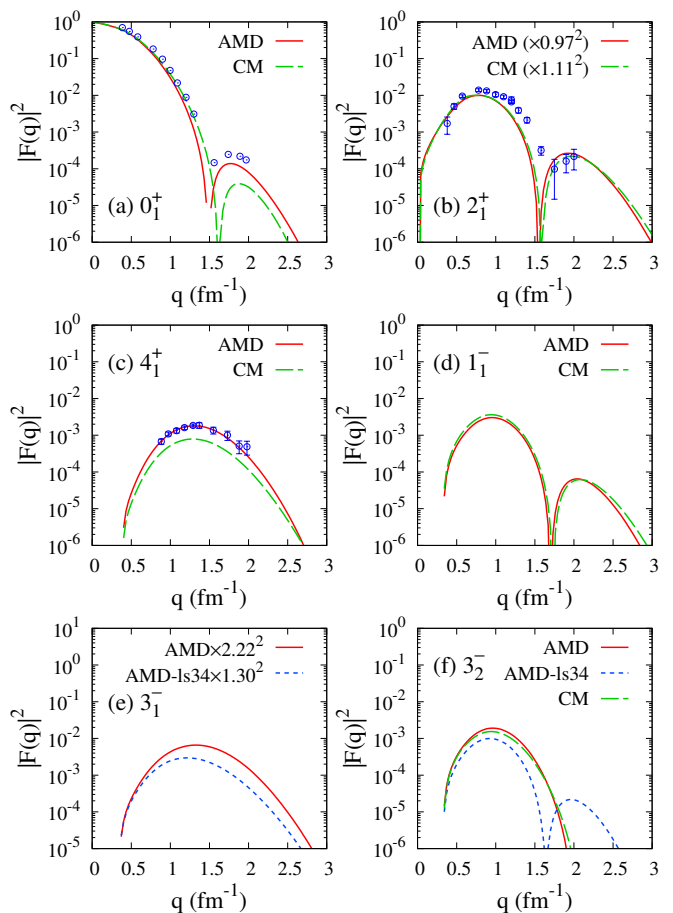


FIG. 4: Elastic and inelastic form factors of ^{20}Ne calculated with AMD (red solid lines) and CM (green dashed lines) compared with the experimental data (circles). The 3_1^- and 3_2^- form factors calculated with AMD-ls34 (blue dotted lines) are also shown in panels (e) and (f), respectively. The theoretical 2_1^+ form factors obtained by AMD (CM) are renormalized by $f^{\text{tr}} = 0.97$ (1.11). The theoretical 3_1^- form factors obtained by AMD and AMD-ls34 are multiplied by $f^{\text{tr}} = 2.22$ and 1.30, respectively. The experimental data are those measured by electron scattering [58].

dependence of matter densities is not so strong. The calculated form factors and transition densities are shown in Figs. 4 and 5, respectively. For the $2_1^+ \rightarrow 0_1^+$ and $3_1^- \rightarrow 0_1^+$ transitions, theoretical values are renormalized with f^{tr} determined from the experimental and theoretical $B(E\lambda)$ values listed in Table II. The experimental form factors observed by (e, e') scattering are also shown in Figs. 4(a), (b), and (c). The AMD and CM calculations reproduce the elastic form factors, and also describe the inelastic form factors to the 2_1^+ state. The calculated 4_1^+ form factors obtained with AMD are in good agreement with the (e, e') data, but those with CM underestimates the data (see Fig. 4(c)).

In the AMD result for $E3$ transitions, clear differences between the 3_1^- and 3_2^- states can be seen in the form factors and transition densities, which are shown by red

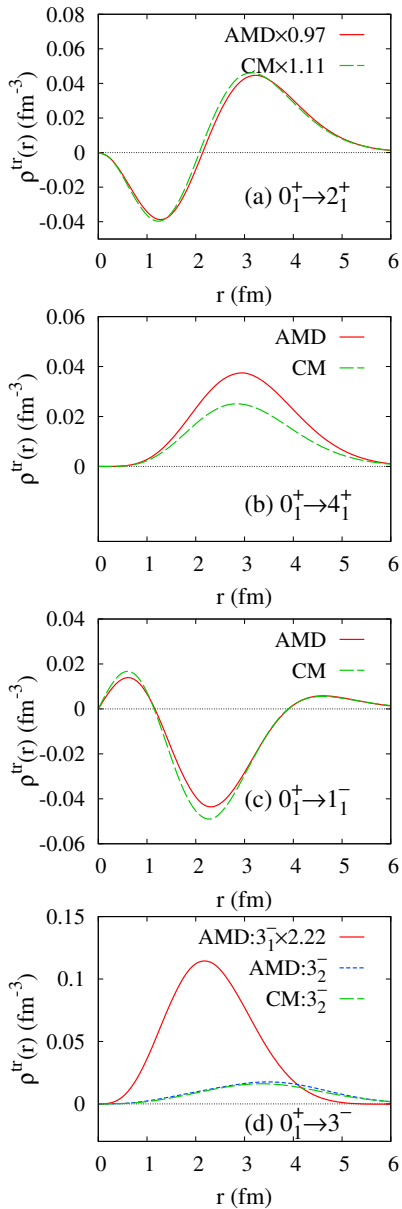


FIG. 5: Transition densities of ^{20}Ne calculated with AMD and CM. Theoretical values obtained by AMD (CM) for the 2_1^+ state are renormalized by $f^{\text{tr}} = 0.97$ (1.11), and those for 3_1^- state are multiplied by $f^{\text{tr}} = 2.22$.

lines of Figs. 4(e), 4(f), and 5(d). The 3_1^- form factors have the higher peak at a larger q , while the 3_2^- form factors show the lower peak at a smaller q . Similarly, one can see the difference also in the transition densities: narrower distributions of the $3_1^- \rightarrow 0_1^+$ transition densities and broader distributions with the outer tail of the $3_2^- \rightarrow 0_1^+$ transition densities because of the developed $^{16}\text{O} + \alpha$ cluster structure. One can say again that the $E3$ form factors and transition densities are sensitive to the state mixing between the $K^\pi = 2^-$ and $K^\pi = 0_1^-$ bands. Detailed discussions of its effect are given in Sec. V.

IV. PROTON AND α SCATTERING

The MCC calculations with AMD and CM are performed for proton scattering at incident energies of $E_p = 25, 30,$ and 35 MeV and α scattering at $E_\alpha = 104, 146,$ and 386 MeV. To see the coupled channel (CC) effect, the one-step calculation of the distorted wave born approximation (DWBA) is also performed using the AMD densities. As described previously, the theoretical transition densities are renormalized by multiplying the factors (f^{tr}), which are determined as $f^{\text{tr}} = \sqrt{B_{\text{exp}}(E\lambda)/B_{\text{th}}(E\lambda)}$ to fit the experimental data of $B(E2; 2_1^+ \rightarrow 0_1^+)$, $B(E2; 4_1^+ \rightarrow 2_1^+)$, $B(E2; 3_2^- \rightarrow 1_1^-)$, and $B(E3; 3_1^- \rightarrow 0_1^+)$. For the $E2; 2_1^+ \rightarrow 2_1^+$ transition, f^{tr} is chosen to adjust the theoretical $Q(2_1^+)$ to the experimental value. For other transitions, $f^{\text{tr}} = 1$ (no renormalization) is used.

The calculated cross sections of proton elastic and inelastic scattering are shown in Fig. 6 compared with the experimental data. The MCC+AMD (red solid lines) and MCC+CM (green dashed lines) reproduce the 0_1^+ and 2_1^+ cross sections data well at the first and second peaks. For the 4_1^+ cross sections, the observe data do not show clear peak structures enough to discuss diffraction patterns. The MCC+AMD reasonably reproduces the global amplitudes of the 4_1^+ data, while the MCC+CM gives smaller 4_1^+ cross sections than MCC+AMD and the data because of the weaker $E4$ transition than AMD result. The 1_1^- cross sections are reasonably described with the MCC+AMD and MCC+CM calculations except for forward angles. As for the 3_1^- cross sections, the MCC+AMD reproduces the first peak amplitude of the data, but somewhat overestimates the second peak amplitude. In comparison of the DWBA+AMD (blue dotted lines) and MCC+AMD (red solid lines) calculations, non-negligible CC effects are seen in this energy range $E_p = 25\text{--}35$ MeV except for the 3_1^- state.

The α elastic and inelastic cross sections are shown in Fig. 7. The calculated cross sections are compared with the experimental data. For the elastic scattering (Fig. 7(a)), the $E_\alpha = 104$ MeV data from Ref. [30] are reproduced well by MCC+AMD (red solid lines) and MCC+CM (green dashed lines) except for backward angles, whereas the $E_\alpha = 386$ MeV data from Ref. [31] are about two times smaller than the present MCC calculations. We do not know the reason for this apparent inconsistency, but uncertainty from the present reaction model is unlikely because its applicability to α elastic scattering at $E_\alpha = 100\text{--}400$ MeV has been already examined for various target nuclei [32–35, 50, 54]. Therefore, it is likely that the $E_\alpha = 386$ MeV data in Ref. [31] contains uncertainty of the normalization. Assuming the normalization to be an overall factor of two, we multiply the original (α, α) and (α, α') data of Ref. [31] by this factor, and obtain excellent agreement of the calculations with the (α, α) data as shown in Fig. 7(a). Also the 2_1^+ cross sections at $E_\alpha = 104\text{--}386$ MeV are well reproduced by the MCC+AMD and MCC+CM calcula-

tions. For the 4_1^+ cross sections, the MCC+AMD result seems better than the MCC+CM result. For the 1_1^- and 3_1^- cross sections, there is no data for individual states at $E_\alpha = 104$ MeV, but the cross sections at $E_x = 5.7$ MeV were reported by the $E_\alpha = 104$ MeV experiment in Ref. [30]. The data may contain the 1_1^- (5.79 MeV) and 3_1^- (5.62 MeV) contributions, but they can not be described by a simple sum of the calculated 1_1^- and 3_1^- cross sections of the present calculations. The $E_\alpha = 386$ MeV data of the 3_1^- cross sections are somewhat overestimated by the MCC+AMD calculation, in particular, at the second peak. In comparison of the MCC+AMD (red solid lines) and DWBA+AMD (blue dotted lines) calculations for α scattering, one can see non-negligible CC effect, in particular, at $E_\alpha = 104$ MeV, but the CC effect becomes weaker at $E_\alpha = 386$ MeV.

V. DISCUSSION

As discussed in previous sections, the structure calculation of AMD-ls34 with the modified spin-orbit strength suggests possible state mixing between the $K^\pi = 2^-$ and $K^\pi = 0_1^-$ bands in the 3_1^- and 3_2^- states of ^{20}Ne . Let us remind that the default AMD calculation gives almost no state mixing and obtains the theoretical value of $B(E3; 3_1^- \rightarrow 0_1^+) = 53 e^2\text{fm}^4$ much smaller than the experimental value of $260 \pm 90 e^2\text{fm}^4$. In the AMD-ls34 result, the $K^\pi = 2^-$ band comes down to the lower energy than the $K^\pi = 0_1^-$ band consistently with the experimental energy spectra, and the state mixing occurs between the 3_1^- ($K^\pi = 2^-$) and 3_2^- ($K^\pi = 0_1^-$) states. As a consequence of mixing of the $K^\pi = 0_1^-$ cluster component in the 3_1^- ($K^\pi = 2^-$) state, the theoretical $B(E3; 3_1^- \rightarrow 0_1^+)$ value is enhanced to be $B(E3; 3_1^- \rightarrow 0_1^+) = 155 e^2\text{fm}^4$ being in better agreement with the experimental value.

This state mixing between the 3_1^- and 3_2^- states affects the $E3$ form factors and transition densities. The AMD (red solid lines) and AMD-ls34 (blue dotted lines) results for the form factors are compared in Figs. 4(e) and (f), and those for the transition densities are compared in Fig. 8. In these figures, the 3_1^- form factors and transition densities are renormalized with $f^{\text{tr}} = 2.22$ for AMD and $f^{\text{tr}} = 1.30$ for AMD-ls34 so as to fit the data of $B(E3; 3_1^- \rightarrow 0_1^+)$. Namely, the renormalized 3_1^- transition densities of the two calculations (AMD and AMD-ls34) in Fig. 8 give the same value of $B(E3; 3_1^- \rightarrow 0_1^+) = 260 e^2\text{fm}^4$. Nevertheless, behaviors of the transition densities are different between the AMD and AMD-ls34 results. For the 3_1^- transition densities (Figs. 8(a) and (b)), AMD-ls34 gives a lower peak amplitude in the inner region ($r = 2-3$ fm) and a longer tail in the outer region ($r \sim 5$ fm) because of the mixing of the $K^\pi = 0_1^-$ cluster component. As a result, in the 3_1^- form factors of AMD-ls34, the peak amplitude gets smaller and the peak position shifts to a smaller q (see the blue dotted line of Fig. 4(e)). Also the 3_2^- transition densities are strongly affected by the state mixing as shown in Fig. 8(c). Be-

cause of the destructive mixing of the $K^\pi = 2^-$ component, inner amplitudes in the $r < 3$ fm region are suppressed and the outer peak around $r = 3-4$ fm gets smaller and shifts outwards in AMD-ls34 (blue dotted lines) than in AMD (red solid lines).

The mixing of the $K^\pi = 2^-$ and $K^\pi = 0_1^-$ bands also affects the 3_1^- and 3_2^- cross sections of proton and α inelastic scattering via the transition densities. In Fig. 9, the 3_1^- and 3_2^- cross sections calculated with AMD and AMD-ls34, and experimental data are compared. For the (p, p') cross sections at $E_p = 25$ and 35 MeV, the AMD-ls34 calculation obtains smaller cross sections of the 3_1^- and 3_2^- states than the original AMD result. In particular, the suppression at the second peak of the 3_1^- cross sections is remarkable and shows a better agreement with the 3_1^- data at $E_p = 25$ MeV. The 3_2^- cross sections are suppressed in the whole region of angles. As a result, the agreement with the 3_2^- data is improved at the first peak but gets somewhat worse at the second peak.

For α scattering to the 3_1^- state, peak positions shift to forward angles in the AMD-ls34 result probing the longer tail of the transition densities, which is caused by mixing of the $K^\pi = 0_1^-$ cluster component. Compared to the experimental 3_1^- cross sections at $E_\alpha = 386$ MeV, a good agreement is obtained by AMD-ls34. This result may support significant mixing of the $K^\pi = 0_1^-$ cluster component in the 3_1^- ($K^\pi = 2^-$) state. For the (α, α') cross sections at $E_\alpha = 104$ MeV, the data observed for 5.7 MeV are not enough of high quality to discuss detailed features of the 3_1^- state because they contain large uncertainty from the 1_1^- contribution. As for the 3_2^- cross sections, the AMD-ls34 result predicts smaller cross sections than the AMD result because of the destructive mixing of the $K^\pi = 2^-$ component in the 3_2^- ($K^\pi = 0_1^-$) state.

In the present analysis with AMD and AMD-ls34, we can say that possible mixing of the $K^\pi = 0_1^-$ cluster component in the 3_1^- state can be probed by proton and α cross sections through the transition densities. The better agreements of the AMD-ls34 result with the (p, p') data at $E_p = 25$ MeV and (α, α') data at $E_\alpha = 386$ MeV supports the significant outer tail of the 3_1^- transition densities and favors the state mixing case. For the 3_2^- state, experimental data are not enough to draw an answer to the state mixing in the 3_2^- state.

VI. SUMMARY

The structure and transition properties of the $K^\pi = 0_1^+$, $K^\pi = 2^-$, and $K^\pi = 0_1^-$ bands of ^{20}Ne were investigated with the microscopic structure and reaction calculations via proton and α scattering off ^{20}Ne .

In the structure calculation of ^{20}Ne with AMD, $^{16}\text{O} + \alpha$ cluster structures were obtained in the parity-doublet $K^\pi = 0_1^+$ and $K^\pi = 0_1^-$ bands, and the $^{12}\text{C} + 2\alpha$ -like structure was obtained in the $K^\pi = 2^-$ band. The AMD calculation reproduced the experimental $B(E2)$ of

in-band transitions. It also described the experimental form factors of the 0_1^+ , 2_1^+ , and 4_1^+ states.

The MCC calculations with the Melbourne g -matrix NN interaction were performed for proton and α scattering off ^{20}Ne using the AMD densities of ^{20}Ne . The MCC calculations reasonably reproduced the observed cross sections of proton scattering at $E_p = 25\text{--}35$ MeV and α scattering at $E_\alpha = 104\text{--}386$ MeV. Transition properties from the ground to excited states were discussed via the reaction analyses of proton and α inelastic processes.

The mixing of the $K^\pi = 2^-$ and $K^\pi = 0_1^-$ bands in the 3_1^- and 3_2^- states was investigated in the analyses of AMD (default) with almost no mixing and AMD-ls34 (a modified spin-orbit strength) with the state mixing. The former calculation (AMD) significantly underestimates the experimental $B(E3; 3_1^- \rightarrow 0_1^+)$, while the latter (AMD-ls34) calculation obtains a better result for $B(E3; 3_1^- \rightarrow 0_1^+)$ because the $E3$ transition strength is enhanced by mixing of the $K^\pi = 0_1^-$ cluster component. The state mixing of the $3_1^- (K^\pi = 2^-)$ and $3_2^- (K^\pi = 0_1^-)$ states also affects the $E3$ transition densities from the ground state, which can be probed by (p, p') and (α, α') cross sections, in principle. The detailed analysis of proton and α cross sections for the 3_1^- and 3_2^- states

was performed by the MCC calculations with AMD and AMD-ls34. The observed (p, p') data at $E_p = 25$ MeV and (α, α') data at $E_\alpha = 386$ MeV seems to support the mixing of the $K^\pi = 0_1^-$ cluster component in the $3_1^- (K^\pi = 2^-)$ state.

It should be commented that applicability of the present MCC approach with the Melbourne g -matrix NN interaction for low-energy proton scattering in the $E_p \lesssim 30$ MeV range has not been well examined yet. In order to clarify the properties of the 3_1^- and 3_2^- states, further detailed data of proton and α scattering at various energies are needed.

Acknowledgments

The authors thank Dr. Kimura and Dr. Kawabata for fruitful discussions. The computational calculations of this work were performed by using the supercomputer in the Yukawa Institute for theoretical physics, Kyoto University. This work was partly supported by Grants-in-Aid of the Japan Society for the Promotion of Science (Grant Nos. JP18K03617, JP16K05352, and 18H05407) and by the grant for the RCNP joint research project.

-
- [1] Y. Fujiwara *et al.*, Prog. Theor. Phys. Suppl. **68**, 29 (1980).
 - [2] H. Horiuchi and K. Ikeda, Prog. Theor. Phys. **40**, 277 (1968).
 - [3] B. Buck, J. C. Johnston, A. C. Merchant and S. M. Perez, Phys. Rev. C **52**, 1840 (1995).
 - [4] W. Sünkel, K. Wildermuth, Phys. Lett. **B41**, 439 (1972).
 - [5] F. Nemoto and H. Bandō, Prog. Theor. Phys. **47**, 1210 (1971).
 - [6] F. Nemoto, Y. Yamamoto, H. Horiuchi, Y. Suzuki, K. Ikeda, Prog. Theor. Phys. **54**, 104 (1975).
 - [7] T. Matsuse, M. Kamimura, and Y. Fukushima, Prog. Theor. Phys. **49**, 1765 (1973).
 - [8] T. Matsuse, M. Kamimura, and Y. Fukushima, Prog. Theor. Phys. **53**, 706 (1975).
 - [9] Y. Fujiwara, H. Horiuchi, R. Tamagaki Prog. Theor. Phys. **61**, 1629 (1979).
 - [10] Y. Fujiwara Prog. Theor. Phys. **62**, 122 (1979).
 - [11] Y. Fujiwara Prog. Theor. Phys. **62**, 138 (1979).
 - [12] M. Dufour, P. Descouvemont and D. Baye, Phys. Rev. C **50**, 795 (1994).
 - [13] B. Zhou *et al.*, Phys. Rev. C **86**, 014301 (2012).
 - [14] B. Zhou *et al.*, Phys. Rev. Lett. **110**, no. 26, 262501 (2013).
 - [15] Y. Kanada-En'yo and H. Horiuchi, Prog. Theor. Phys. **93**, 115 (1995).
 - [16] M. Kimura, Phys. Rev. C **69**, 044319 (2004).
 - [17] N. Itagaki, J. Cseh and M. Ploszajczak, Phys. Rev. C **83**, 014302 (2011).
 - [18] Y. Taniguchi, M. Kimura and H. Horiuchi, Prog. Theor. Phys. **112**, 475 (2004).
 - [19] H. Ohta, K. Yabana and T. Nakatsukasa, Phys. Rev. C **70**, 014301 (2004).
 - [20] S. Shinohara, H. Ohta, T. Nakatsukasa and K. Yabana, Phys. Rev. C **74**, 054315 (2006).
 - [21] E. F. Zhou, J. M. Yao, Z. P. Li, J. Meng and P. Ring, Phys. Lett. B **753**, 227 (2016).
 - [22] P. Marevi, J. P. Ebran, E. Khan, T. Niki and D. Vretenar, Phys. Rev. C **97**, no. 2, 024334 (2018).
 - [23] J. Hiura and F. Nemoto, and H. Bandō, Prog. Theor. Phys. Suppl. **52**, 173 (1972).
 - [24] O. Husser, T. K. Alexander, A. B. McDonald, G. T. Ewan and A. E. Litherland, Nucl. Phys. A **168**, 17 (1971).
 - [25] F. Hinterberger, G. Mairle, U. Schmidt-Rohr, G. J. Wagner and P. Turek, Nucl. Phys. A **115**, 570 (1968).
 - [26] R. De Swiniarski, J. Sherman, D. L. Hendrie, C. Glashauser, and A. D. Bacher, Helvetica Physica Acta **49**, 241 (1976).
 - [27] R. De Swiniarski, A. Genoux-Lubain, G. Bagieu, J. F. Cavaignac, D. H. Worledge and J. Raynal, Phys. Lett. **43B**, 27 (1973).
 - [28] R. de Swiniarski, F. G. Resmini, D. L. Hendrie and A. D. Bacher, Nucl. Phys. A **261**, 111 (1976).
 - [29] G. S. Blanpied, B. G. Ritchie, M. L. Barlett, R. W. Ferguson, G. W. Hoffmann, J. A. McGill and B. H. Wildenthal, Phys. Rev. C **38**, 2180 (1988).
 - [30] H. Rebel, G. W. Schweimer, G. Schatz, J. Specht, R. Lhken, G. Hauser, D. Habs and H. Klewe-Nebenius, Nucl. Phys. A **182**, 145 (1972).
 - [31] S. Adachi *et al.*, Phys. Rev. C **97**, no. 1, 014601 (2018).
 - [32] Y. Kanada-En'yo and K. Ogata, Phys. Rev. C **99**, no. 6, 064601 (2019).
 - [33] Y. Kanada-En'yo and K. Ogata, Phys. Rev. C **99**, no. 6,

- 064608 (2019).
- [34] Y. Kanada-En'yo and K. Ogata, *Phys. Rev. C* **100**, no. 6, 064616 (2019).
- [35] Y. Kanada-En'yo and K. Ogata, arXiv:2002.02625 [nucl-th].
- [36] K. Amos, P. J. Dortmans, H. V. von Geramb, S. Karataglidis, and J. Raynal, *Adv. Nucl. Phys.* **25**, 275 (2000).
- [37] R. Machleidt, K. Holinde, and Ch. Elster, *Phys. Reports* **149**, 1 (1987).
- [38] Y. Kanada-En'yo, H. Horiuchi and A. Ono, *Phys. Rev. C* **52**, 628 (1995).
- [39] Y. Kanada-En'yo, *Phys. Rev. Lett.* **81**, 5291 (1998).
- [40] Y. Kanada-En'yo, M. Kimura and A. Ono, *Prog. Theor. Exp. Phys.* **2012** 01A202 (2012).
- [41] Y. Kanada-En'yo, H. Horiuchi and A. Dote, *Phys. Rev. C* **60**, 064304 (1999).
- [42] Y. Kanada-En'yo and H. Horiuchi, *Phys. Rev. C* **68**, 014319 (2003).
- [43] D. L. Hill and J. A. Wheeler, *Phys. Rev.* **89**, 1102 (1953);
- [44] J. J. Griffin and J. A. Wheeler, *Phys. Rev.* **108**, 311 (1957).
- [45] Y. Kanada-En'yo, *Phys. Rev. C* **96**, 034306 (2017).
- [46] T. Ando, K. Ikeda, and A. Tohsaki, *Prog. Theor. Phys.* **64**, 1608 (1980).
- [47] R. Tamagaki, *Prog. Theor. Phys.* **39**, 91 (1968).
- [48] N. Yamaguchi, T. Kasahara, S. Nagata, and Y. Akaishi, *Prog. Theor. Phys.* **62**, 1018 (1979).
- [49] D. M. Brink, International School of Physics "Enrico Fermi", XXXVI, p. 247, Academic Press, New York and London (1966).
- [50] K. Egashira, K. Minomo, M. Toyokawa, T. Matsumoto and M. Yahiro, *Phys. Rev. C* **89**, 064611 (2014).
- [51] K. Minomo, K. Ogata, M. Kohno, Y. R. Shimizu and M. Yahiro, *J. Phys. G* **37**, 085011 (2010).
- [52] M. Toyokawa, K. Minomo, and M. Yahiro, *Phys. Rev. C* **88**, 054602 (2013).
- [53] K. Minomo, K. Washiyama and K. Ogata, arXiv:1712.10121 [nucl-th].
- [54] K. Minomo and K. Ogata, *Phys. Rev. C* **93**, 051601(R) (2016).
- [55] M. Toyokawa, M. Yahiro, T. Matsumoto, K. Minomo, K. Ogata and M. Kohno, *Phys. Rev. C* **92**, no. 2, 024618 (2015) Erratum: [*Phys. Rev. C* **96**, 059905(E) (2017)].
- [56] I. Angeli and K. P. Marinova, *At. Data Nucl. Data Tables* **99**, 69 (2013).
- [57] D. R. Tilley, C. M. Cheves, J. H. Kelley, S. Raman and H. R. Weller, *Nucl. Phys. A* **636**, 249 (1998).
- [58] Y. Horikawa, Y. Torizuka, A. Nakada, S. Mitsunobu, Y. Kojima and M. Kimura, *Phys. Lett.* **36B**, 9 (1971).
- [59] E. Fabrici, S. Micheletti, M. Pignanelli, F. G. Resmini, R. De Leo, G. D'Erasmus and A. Pantaleo, *Phys. Rev. C* **21**, 844 (1980).
- [60] K. T. Knipfle, G. J. Wagner, A. Kiss, M. Rogge, C. Mayer-Bricke and T. Bauer, *Phys. Lett.* **64B**, 263 (1976).

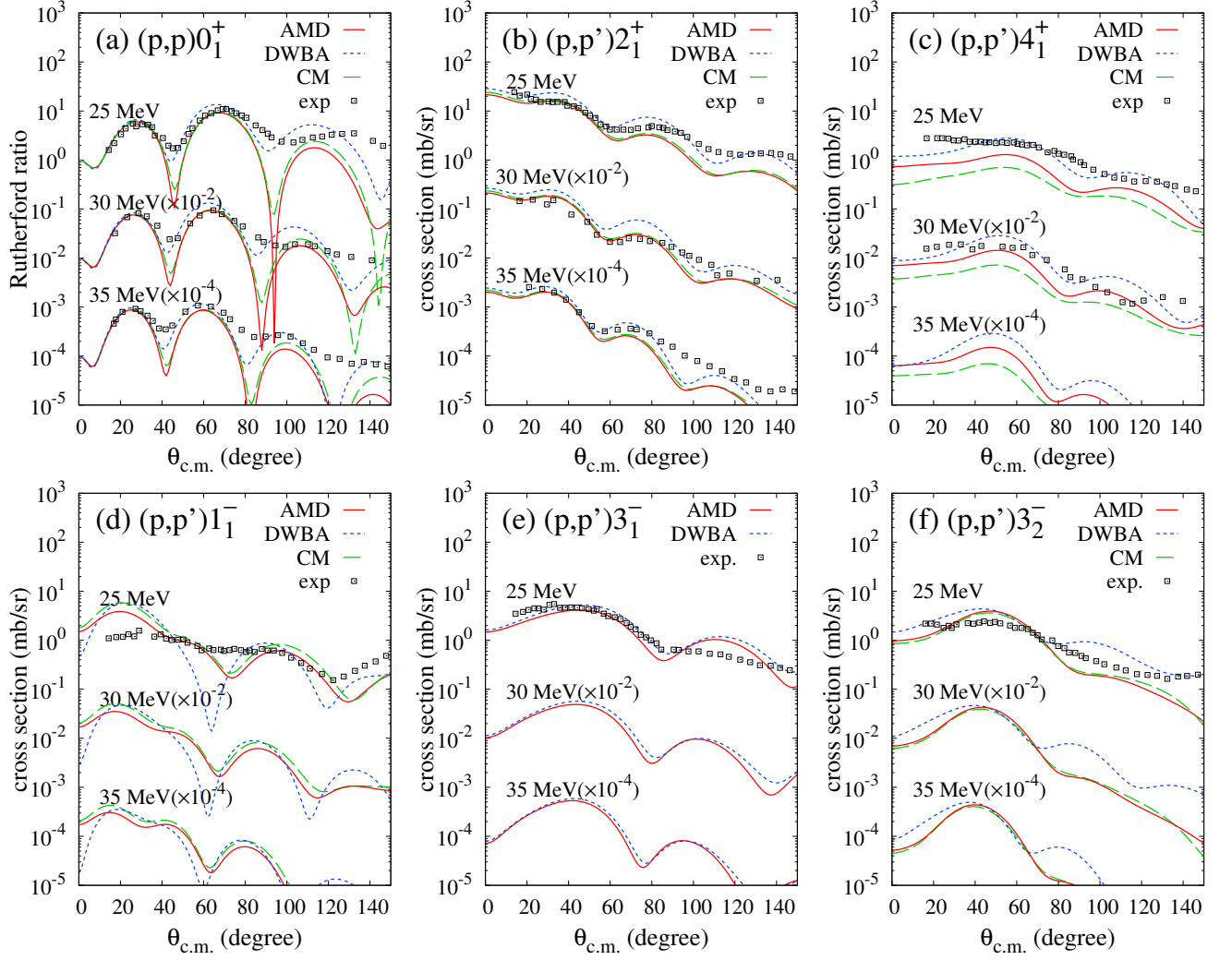


FIG. 6: Cross sections of proton elastic and inelastic scattering off ^{20}Ne at incident energies of $E_p = 25, 30,$ and 35 MeV calculated with MCC+AMD (red solid lines), DWBA+AMD (blue dotted lines), and MCC+CM (green dashed lines), which are labeled as AMD, DWBA, and CM, respectively. Experiment data are cross sections at $E_p = 24.5$ MeV [26, 28], 30 MeV [28], and 35 MeV [59].

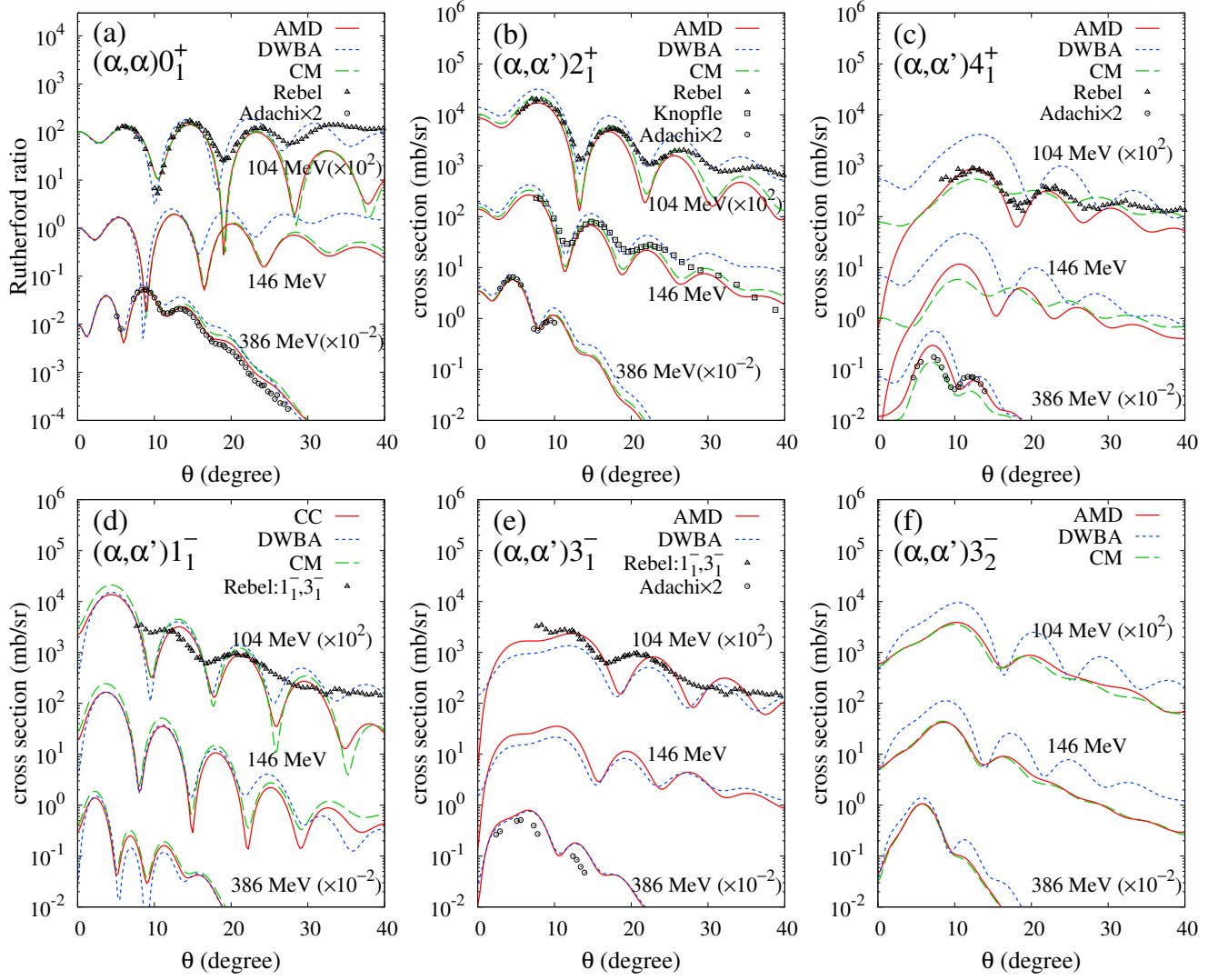


FIG. 7: Cross sections of α elastic and inelastic scattering off ^{20}Ne at incident energies of $E_\alpha = 104, 146,$ and 386 MeV calculated with MCC+AMD (red solid lines), DWBA+AMD (blue dotted lines), and MCC+CM (green dashed lines), which are labeled as AMD, DWBA, and CM, respectively. Experiment data are cross sections at $E_\alpha = 104$ MeV [30], and 146 MeV [60], and 386 MeV [31]. The $E_\alpha = 386$ MeV data from Ref. [31] are multiplied by a factor of two. The (α, α') data at $E_\alpha = 104$ MeV in the panels (d) and (e) are the cross sections observed for $E_x = 5.7$ MeV and may contain 1_1^- (5.79 MeV) and 3_1^- (5.62 MeV) contributions.

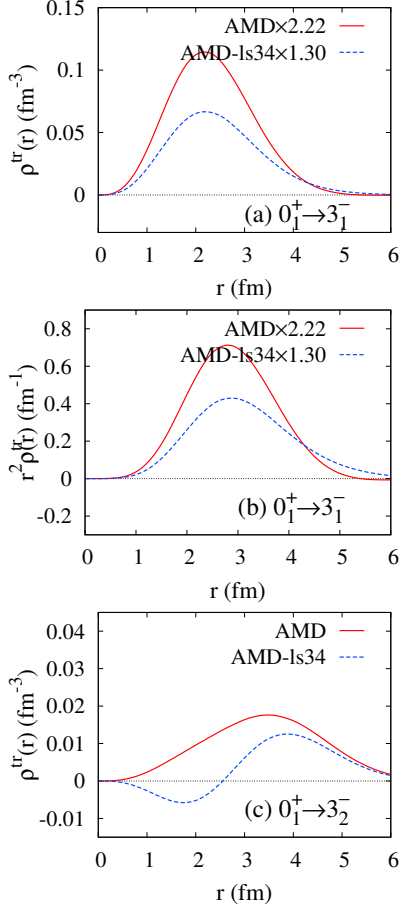


FIG. 8: Transition densities from the ground to 3^- states obtained with AMD (default) and AMD-ls34 (modified spin-orbit strength). (a) transition densities to the 3_1^- state, (b) those but r^2 -weighted, (b) transition densities to the 3_2^- state. Transition densities to the 3_1^- state in (a) and (b) are renormalized by $f_{tr} = 2.22$ for AMD and 1.30 for AMD-ls34.

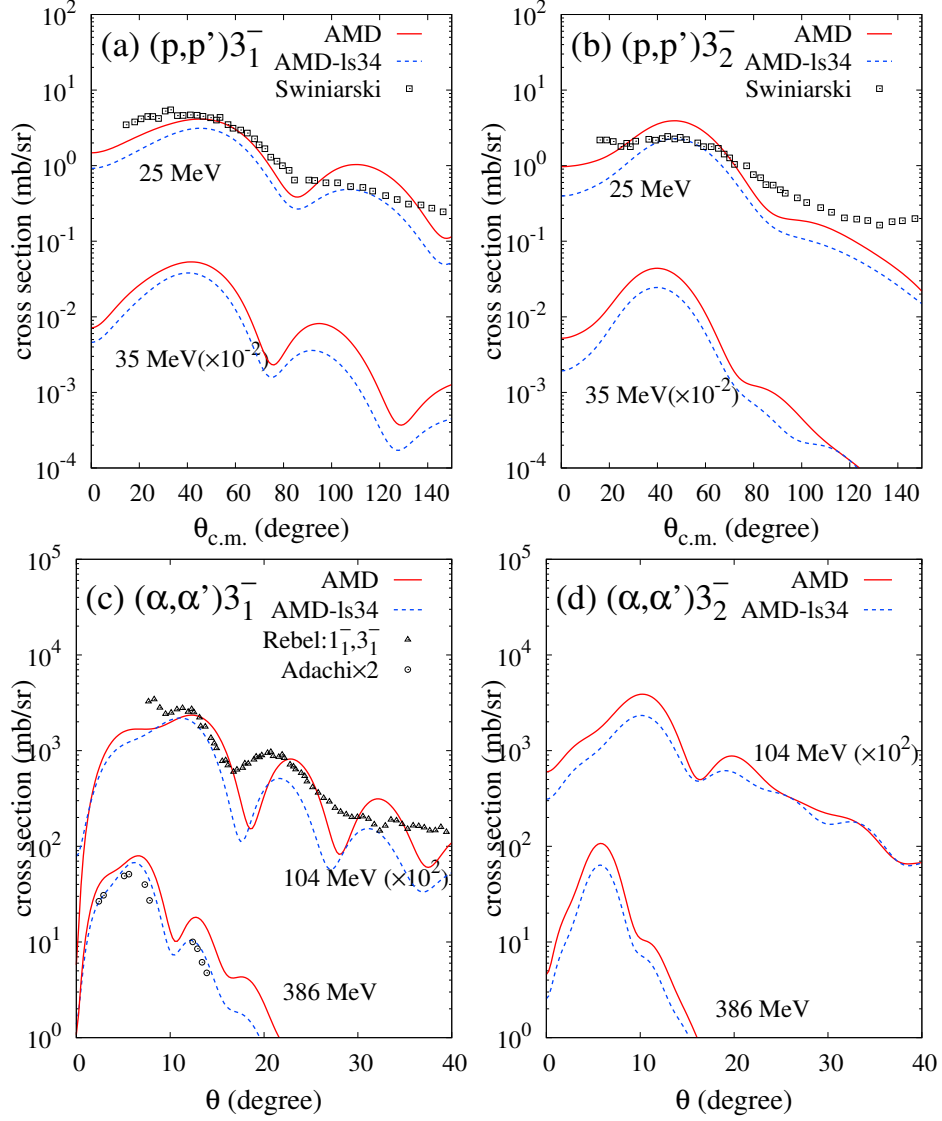


FIG. 9: Cross sections of proton and α inelastic scattering calculated with MCC using the AMD (default) and AMD-ls34 (modified spin-orbit strength) densities, and the experimental cross sections. The (p, p') cross sections at $E_p = 25$ and 35 MeV to the (a) 3_1^- and (b) 3_2^- states and the (α, α') cross sections at $E_\alpha = 146$, and 386 MeV to the (c) 3_1^- and (d) 3_2^- states. The (p, p') data at $E_p = 24.5$ MeV [28] and (α, α') data at $E_\alpha = 104$ MeV [30] and 386 MeV [31] are also shown. The (α, α') data at 386 MeV of Ref. [31] are multiplied by a factor of two. The (α, α') data at $E_\alpha = 104$ MeV in the panel (c) are not cross sections for an individual state but may contain 1_1^- and 3_1^- contributions around 5.7 MeV.